Influence of plastic deformation on the magnetic properties of Heusler $MnAu_2Al$

Emily E. Levin,[1] Daniil A. Kitchaev,[1] Yolita M. Eggeler,[1,2] Justin A. Mayer,[1] Piush Behera,[1] Daniel S. Gianola,[1] Anton Van der Ven,[1] Tresa M. Pollock,[1] and Ram Seshadri[1,3,*]

[1]*Materials Department and Materials Research Laboratory, University of California, Santa Barbara, California 93106, USA*

[2]*Laboratory for Electron Microscopy, Karlsruhe Institute of Technology, D-76131 Karlsruhe, Germany*

[3]*Department of Chemistry and Biochemistry, University of California, Santa Barbara, California 93106, USA*

(Received 23 September 2020; accepted 9 December 2020; published 15 January 2021)

The Heulser intermetallic $MnAu_2Al$ is shown to undergo a dramatic change in net magnetization in response to plastic deformation. A mechanism is proposed involving antiferromagnetic interactions in the otherwise ferromagnetic compound (when ordered) that arise due to chemical changes at the antiphase boundaries created by the deformation. The coupling between chemical and magnetic order across antiphase boundaries is likely to occur in other ordered magnetic systems and may provide an explanation for otherwise anomalous magnetic behavior across several systems, including other Heusler intermetallics.

DOI: 10.1103/PhysRevMaterials.5.014408

I. INTRODUCTION

For material systems in which magnetic interactions depend strongly on local order and interatomic distances, mechanical deformation can lead to a wide range of interesting magnetic phenomena. The coupling between mechanics and magnetism is particularly evident in ordered intermetallics that undergo plastic deformation, where dislocations may place atoms on new atomic sites, and therefore create new chemical environments and interatomic distances. We examine this phenomenon in Heusler $MnAu_2Al$, wherein we derive the atomistic mechanism underlying the strong dependence of bulk magnetic properties on defects induced through plastic deformation.

Heusler intermetallics crystallize in the $L2_1$ structure in space group $Fm\bar{3}m$, and have the chemical formula XY_2Z where, respectively X and Y are usually an earlier and later transition metal, and Z is a main group element. Friedrich Heusler first discovered this family of compounds in 1903, noting the ordered structure $MnCu_2Al$ was ferromagnetic, despite none of the constituent elements exhibiting ferromagnetism [1]. Since then, Mn-based Heuslers with the general formula MnY_2Z have proven to be a diverse class of materials that include ferromagnets, ferrimagnets, and antiferromagnets with the particular magnetic order sensitive to valence electron count [2,3].

A simple model often used to explain the magnetic order observed in Mn-based Heuslers assumes the Y and Z elements are nonmagnetic. The magnetism is then attributed to localized magnetic moments on the Mn atoms that couple to one another *via* Ruderman-Kittel-Kasuya-Yosida exchange facilitated by the Z element [4–6]. Although this simple model fails to acknowledge the importance of direct magnetic exchange, where magnetic atoms couple to one another on neighboring sublattices [7,8], it provides a foundation for understanding the oscillation between ferromagnetic and antiferromagnetic exchange within Mn-based Heuslers. This phenomenon has been experimentally verified by inelastic neutron scaterring performed by Noda and Ishikawa on $MnNi_2Sn$ and $MnPd_2Sn$ [9], and Tajima *et al.* on $MnCu_2Al$ [10].

The oscillatory nature of the magnetic exchange interactions as a function of interatomic distance, as well as local chemical order, indicates the relative strength of ferromagnetic and antiferromagnetic magnetic exchange within Heuslers can be impacted by planar faults and dislocations. This phenomenon has been employed to describe the decrease in bulk magnetization that has been observed after cold working in a number of Heusler alloys including $MnCu_2Al$ and $MnPd_2Sn$ [11–13]. Lorentz transmission electron microscopy performed on $MnCu_2Al$ by Lapworth and Jakubovics [13] provided some of the first substantial evidence of strong antiferromagnetic interactions in the otherwise ferromagnetic $MnCu_2Al$ as it was revealed that magnetic domains were pinned at antiphase boundaries (APBs) generated *via* thermal stress or plastic deformation [13]. A similar behavior was reported for $MnPd_2Sn$ when Shinohara *et al.* observed a seemingly anomalous decrease in bulk magnetization after crushing induction melted $MnPd_2Sn$ into a fine powder [11]. These data were suggested as indirect evidence that Mn atoms across the APBs were coupling antiferromagnetically, although direct evidence of such an atomistic coupling has not been reported.

In this contribution, we resolve the full atomistic mechanism of magnetoplastic coupling in the $MnAu_2Al$ model system for ordered intermetallic ferromagnets in which plastic deformation can disrupt macroscopic magnetic order. We derive the likely chemical structure of defects created by plastic deformation and show that these defects lead to new, antiferromagnetic interactions and the formation of pinned magnetic domain walls. Previous work on $MnAu_2Al$ has led to uncertainty around the material's properties as the saturation

*seshadri@mrl.ucsb.edu

magnetization, Curie temperature and processing conditions have been inconsistently reported [14–19]. Our work highlights the importance of defect induced magnetic exchange in this material when characterizing the macroscopic magnetic properties. The behavior is quantified here by using density functional theory (DFT) to identify the planar defects likely to form during plastic deformation and map out their magnetic configuration as a function of chemical order and Mn–Mn distance. To the best of our knowledge this is the first time coupling between magnetism and plastic deformation has been understood on the basis of the electronic structure at the level of atoms and near-neighbor ordering. X-ray diffraction, magnetic measurements, and transmission electron microscopy on $MnAu_2Al$ are complemented by the detailed DFT calculations here. The calculations then help outline a process for identifying similar ordered intermetallics that may provide a platform for engineering the magnetic domain structure of materials through mechanical means.

II. MATERIALS AND METHODS

Starting materials of cleaned Mn (Alfa Aesar, pieces, 99.99%), Au (Alda Aesar, powder, 99.96%), and Al (Sigma Aldrich, powder, 99.95%) were weighed in a 1.2:2:1 stoichiometry to account for Mn volatilization during melting, and ground for 10 minutes in a mortar and pestle to ensure homogeneity. The mixed powder was pressed into a 6 mm pellet using a force of 2 tons. Sample masses were between 300 and 600 mg. Pellets were arc-melted twice in an Ar atmosphere, flipping the ingot between melts, with mass losses between 0.7% and 3.2%. The ingots were ground into powder and sealed in an evacuated fused silica ampule. The powder was annealed at 500 °C for 6 days, and then slow cooled to room temperature at a rate of 0.5 °C min^{-1}. For samples labeled "annealed," the powder was not ground any further. Samples that have been ground after the 500 °C anneal are referred to as "ground." The ground samples were hand ground with a mortar and pestle for 5 min to 20 min. Additional magnetic and microstructural analysis was performed on an arc-melted polycrystalline ingot that was annealed under the same conditions and then deformed by mechanically pressing in a hydraulic press. The change in thickness of the pressed ingot was measured with calipers and corresponded to a plastic strain of roughly 6.5%.

X-ray diffraction patterns were collected for 30 min on a laboratory diffractometer (Panalytical, Empyrean) using a Cu Kα source ($\lambda = 1.5406$ Å). Pawley refinements were performed in TOPAS [20]. The peak shape fit from the annealed sample, measured under identical conditions to the ground sample, was fit with a Lorentzian function. This peak shape was used as a basis where additional broadening in the ground sample is assigned to size broadening. As peak broadening can be caused by both strain and crystallite size, the diffraction pattern of the ground sample was initially assumed to be due to a convolution between the diffraction pattern of the annealed sample, a pseudo-Voigt function due to crystallite size, and a pseudo-Voigt function due to microstrain. The best fit results from assuming the peak broadening is caused exclusively by a reduction in crystallite size. Crystallite size is then calculated using the integral breadth or full width at half max (FWHM) of diffraction peaks in the ground sample, resulting in a weighted average of crystallite size [21].

Magnetic measurements were performed on a SQUID magnetic property measurement system (MPMS3, Quantum Design) equipped with a vibrating sample magnetometer (VSM). Field-cooled and zero-field-cooled magnetization (M) versus temperature (T) measurements were taken upon warming at a field $H = 20$ mT while sweeping temperature at 5 K min^{-1}. Magnetization was measured as a function of field at $T = 2$ K between $H = -7$ and 7 T.

A detailed microsctructural investigation was performed on an electron transparent lamella micromachined from the mechanically pressed ingot using a focused ion beam incorporated within an FEI Helios Dualbeam Nanolab 600. Transmission electron microscopy (TEM), exploiting multiple imaging modes, was performed in an FEI Talos F200X S/TEM operated at 200 kV. Conventional bright field TEM imaging paired with selected area electron diffraction (SAED) patterns were recorded to acquire representative microstructure images and identify the phases present, respectively. Scanning transmission electron microscopy (STEM) performed using a high angle annular dark field (HAADF) detector was applied to explore and elucidate nanostructural features. Specifically, the HAADF detector was set to a camera length of 95 mm to preferentially collect electrons from elements with large atomic number. Images recorded at this camera length will therefore be referred to as atomic mass sensitive images. Additionally, the HAADF detector was set to a camera length of 440 mm to record images sensitive to strain contrast.

All electronic structure calculations were performed using the Vienna *ab initio* simulation package (VASP) [22–24], using the Perdew–Burke–Ernzerhof (PBE) exchange-correlation functional [25] and the projector-augmented wave (PAW) method [26]. All calculations are converged to 10^{-6} eV in total energy and relied on a reciprocal space discretization of 400 k points per Å^3 (≈6000 k points per atom). Data processing and analysis were performed using the PYMATGEN package [27].

γ-surface calculations of the planar fault energy were performed using supercells with at least 18 Å separation between periodic images of the interface. The interfacial energy was minimized across possible normal displacement [28] at the interface and ferromagnetic versus antiferromagnetic alignment across the interface.

To explore the coupling between magnetic and chemical order in this system, we construct a cluster expansion combining chemical and magnetic degrees of freedom. A cluster expansion builds a quasiclassical, atomistic representation of the configurational energy of a lattice system by summing effective interactions between groups of lattice sites. These interactions between pairs, triplets, etc. of sites depend on the chemical occupation of each site and, if the site is occupied by a magnetic element, its spin orientation. The energy contribution of these effective interactions are determined by fitting the cluster expansion Hamiltonian to energies obtained from electronic structure calculations within density functional theory (DFT), taking care to enforce the invariance to the energy under the symmetries of the system. Further descriptions of this method are available in the literature [29–31].

Of particular value to this work is the fact that a cluster expansion disentangles the coupling between chemical and magnetic order. While a cluster expansion can provide a very precise parametrization of the configurational energy, it is also readily interpretable and comparable to illustrative toy models. This combination of rigor and interpretability allows us to quantify how chemical changes perturb specific magnetic interactions. The cluster expansion Hamiltonian we use has the form

$$E = \sum_{\omega_1} J_{\omega_1} \prod_{i \in \omega_1} \sigma_i + \sum_{(ij)=\omega_2} J_{ij} \sigma_i \sigma_j (S_i \cdot S_j),$$

where ω_1 represents two-, three-, and four-body clusters of sites for the purely chemical part of the Hamiltonian, ω_2 represents pairs of sites for the chemomagnetic part of the Hamiltonian, σ are chemical occupation variables, S are spin unit vectors, and J are fitted interaction coefficients. Pair-interactions up to 8 Å, are included while three- and four-body chemical interactions are only treated within the nearest-neighbor shell. The magnetic couplings are treated to lowest-order, in Heisenberg model form, as a dot-product interaction between spin vectors. We neglect nonlinear pair interactions and all three- and four-spin interactions as the lowest-order Heisenberg model gives satisfactory agreement with DFT in terms of both the relative energy of spin configurations (6 meV/Mn) and the ground-state spin structures for low-energy chemical orderings.

The interactions J are determined by fitting a linear regression between the spin-Hamiltonian and energies obtained from DFT for a wide set of chemical and spin configurations. Specifically, we enumerate chemical orderings with an overall $MnAu_2Al$ stoichiometry up to a supercell of size 8 with respect to the primitive cell of the underlying BCC lattice. For low energy chemical orderings, we then consider all distinct collinear magnetic orderings up to 8 spins per unit cell, and spin-wave configurations with low miller-index propagation vectors. The uncertainty e_i in the value of interaction J_i is determined from $C = F^T F$, the covariance of the regression data matrix F, and $e_i^2 = C_{ii}^{-1} e^2$, where e is the standard error of the fit.

III. RESULTS AND DISCUSSION

X-ray diffraction patterns of the annealed and ground $MnAu_2Al$ powders are shown in Fig. 1. After annealing at 500 °C, sharp peaks located exclusively at the Bragg positions of the cubic $MnAu_2Al$ ordered Heusler structure are observed. When the annealed powder is ground further, the Bragg peaks are broadened. As outlined in the materials and methods, the broadening of diffraction peaks in the ground sample is captured best when attributed to reduction in crystallite size. The calculated average crystallite size is 10.4(1) nm based on integral breadth, or 14.5(2) nm based on FWHM. It should be noted that this value is best interpreted as a lower bound on the crystallite size as it is not possible to completely rule out the presence of strain based on the present laboratory x-ray diffraction data. In particular, in Fig. 1, it is clear that at large Bragg angles the peaks of the ground sample become nearly compromised by the background. This is problematic when attempting to deconvolute strain broadening from crystallite size broadening since broadening caused by strain occurs predominately at large Bragg angles (strain broadening and crystallite broadening vary with respect to Bragg angle as a function of $\tan\theta$ and $1/\cos\theta$, respectively) [21]. It is therefore best to evaluate the presence of microstrained regions within plastically deformed $MnAu_2Al$ based on the electron microscopy results that are presented later on in this contribution.

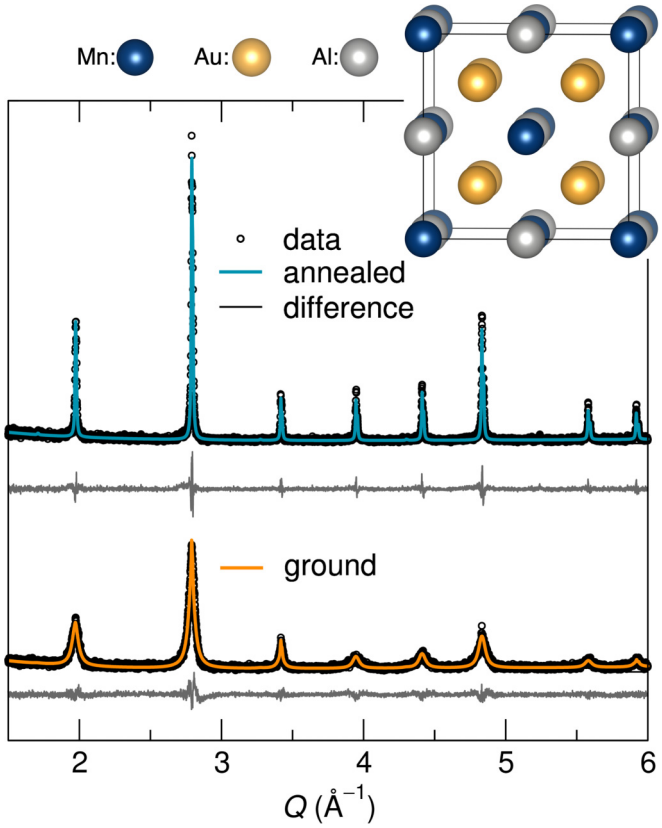

FIG. 1. X-ray diffraction patterns and Pawley refinement fits of annealed and ground $MnAu_2Al$. The annealed sample shows much higher intensity and narrower peak width than after grinding. This peak broadening is due to the nanoscale crystallite size.

The magnetization M as a function of the applied field H, obtained at $T = 2$K are displayed for the annealed and ground powder in Fig. 2(a). The annealed powder shows the characteristic S-shaped curve of a ferromagnet and a saturation magnetization of 3.2 μ_B f.u.$^{-1}$. The curve for the ground powder is not reminiscent of a ferromagnet. Magnetization changes almost linearly with applied field, and there is no saturation magnetization. In addition, Fig. 2(b) demonstrates the annealed sample has a clear Curie temperature, whereas there is no clear magnetic transition after grinding. The magnitude of the magnetization of the ground sample is multiplied by a factor of 100 in order to be viewed on the same axes. Clearly, grinding of $MnAu_2Al$ after the anneal leads to a near zero macroscopic magnetic moment.

This dramatic change in M versus H and M versus T suggests the grinding step modifies the local magnetic ordering in $MnAu_2Al$. To clarify whether this phenomenon is unique to the grinding process, the magnetic properties of a

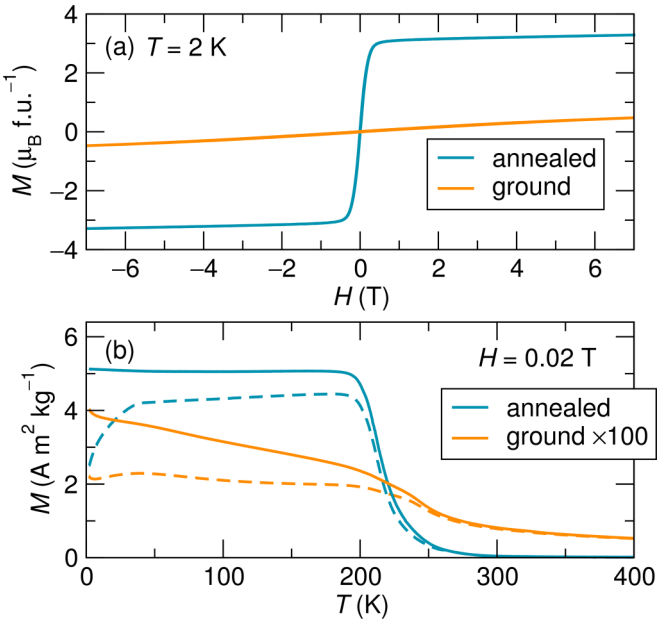

FIG. 2. (a) Magnetization vs applied magnetic field (H) for annealed and ground powders at 2 K. (b) Magnetization vs temperature at $H = 0.02$ T for each. Values of magnetization of the ground powder are multiplied by a factor of 100 so they may be viewed on the same axes. Dotted lines indicate zero-field-cooled measurements.

mechanically pressed ingot of $MnAu_2Al$ were also measured. A plastic strain of approximately 6.5% was imparted on the sample (see methods and materials) and shows a similar decrease in net magnetic moment, although to a lesser extent, as illustrated in Fig. 3. Achieving a strain of this magnitude confirms $MnAu_2Al$ experiences plastic deformation

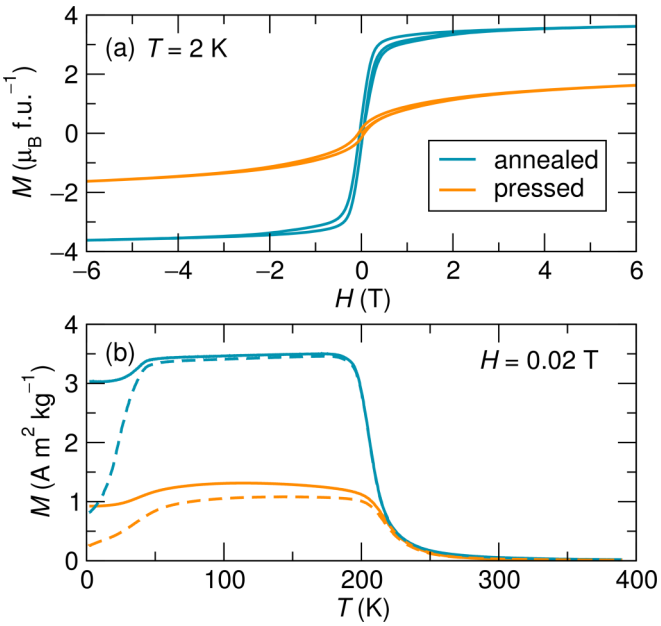

FIG. 3. (a) M vs H at 2 K for an annealed piece and a piece that has been pressed in a hydraulic press after annealing. (b) Magnetization vs temperature at $H = 0.02$ T for each. Dotted lines indicate zero-field-cooled measurements.

before fracture. In result, it is possible for dislocations to be generated in $MnAu_2Al$ via mechanical stress. The observed changes in M versus H and M versus T are therefore expected to be due to plastic deformation caused by the process of grinding annealed powder or pressing an ingot of $MnAu_2Al$. One possible mechanism for this coupling is the generation of APBs during plastic deformation that lead to dramatic decreases in bulk magnetization caused by antiferromagnetic coupling between Mn on an Mn site and Mn on an Al or Au site, similar to the previously observed behavior of the Heusler systems $MnPd_2Sn$ [11,12,32] and $MnCu_2Al$ [13,33]. An alternative explanation is that plastic deformation may induce a change in the magnitude of the local magnetic moment. However, we exclude this possibility because all configurations of $MnAu_2Al$ consistent with the lattice observed in diffraction maintain nearly the same atomic moment magnitude as the pristine $L2_1$ phase.

It is also worth noting in both the annealed powder and the annealed ingot, we observe a downturn in the magnetization below 65 K, indicating the presence of antiferromagnetic interactions below this temperature even in the pristine material. As the downturn in magnetization is limited to the zero-field-cooled data of the annealed powder, the most likely explanation for the anomaly observed within the annealed powder is the formation of anti-aligned ferromagnetic domains. However, since this downturn persists in both the zero-field-cooled and field-cooled data of the annealed ingot, the ingot may very well partially transform into a spiral magnetic phase forming with a lower magnetization, as proposed by Bacon *et al.* [14] They determined using neutron diffraction that part of their sample formed with this spin-spiral structure, and part remained ferromagnetic. This could be due to chemical inhomogeneity or thermal disorder on the Mn and Al site caused by the 500 °C anneal.

To identify characteristic microstructural features of plastically deformed $MnAu_2Al$, we characterize the mechanically pressed ingot using TEM. Conventional TEM bright field imaging in Fig. 4(a) reveals a finely grained microstructure. The corresponding SAED pattern consists of rings that indicate the presence of the Heusler phase and an unidentified secondary phase. Although the exact composition of the secondary phase is unknown, atomic mass contrast HAADF-STEM in Fig. 4(b) reveals the secondary phase consists of 20 nm precipitates that are deficient in Au and located at $MnAu_2Al$ grain boundaries. These precipitates are not expected to contribute to the change in magnetization that is observed in the pressed ingot. If this was the case, it would be expected that the powder diffraction of the ground sample, which is subject to larger stresses than the mechanically pressed ingot, would have a significant phase fraction of this secondary phase.

Strain sensitive HAADF-STEM imaging was also carried out to better understand potential intra-granular features indicative of plastic deformation. A representative microstructural region characterized with this imaging mode is shown in Fig. 4(c), revealing ultrafine elongated grains with a high intra-granular defect density. Ultrafine grain microstructures are often observed in materials that have undergone processing that impart severe plastic deformation onto a specimen such as accumulative roll bonding [34–36], equal-channel

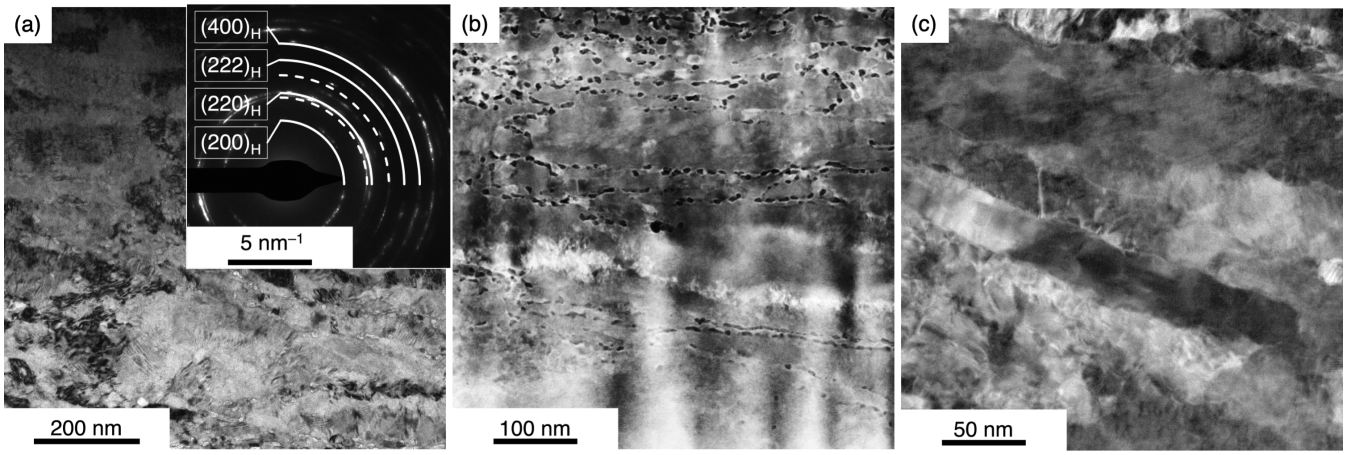

FIG. 4. (a) Bright field TEM micrograph and the corresponding SAED pattern revealing a fine grained microstructure. The diffraction rings identify the Heusler phase (H) and a secondary phase. (b) Atomic mass contrast HAADF-STEM reveals the secondary phase consists of 20-nm Au deficient particulates located at grain boundaries. (c) Strain sensitive HAADF-STEM identifies intra-granular contrast caused by low angle grain boundaries that have formed during plastic deformation.

angular extrusion [37], or a surface mechanical grinding treatment [38]. It is expected that mechanical stress applied by the hydraulic press leads to the formation of low angle grain boundaries (a dense dislocation network). In fact, the variation of the intragranular strain contrast observed, for example, in the center grain of Fig. 4(c) is indicative of a lattice orientation change which presupposes a high density of crystalline defects that form low angle grain boundaries *via* the interaction of a multitude of dislocations.

The combination of x-ray diffraction, magnetic measurements and TEM characterization reveals that both the grinding of annealed powder and pressing of an annealed ingot leads to nanoscale grain refinement. The grain refinement is facilitated by the formation of low energy dislocation structures and therefore will also lead to the formation of a significant density of crystal defects. The dense defect density observed within the mechanically pressed $MnAu_2Al$ ingot makes it difficult to discriminate isolated dislocation dissociation events that lead to the formation of planar defects such as APBs and is not within the scope of this current study. For the sake of clarity, no physical traces of planar defects in the intra-granular regions can be resolved after 6% plastic strain. However, plastic deformation of this magnitude will certainly promote energetically favorable dislocation dissociation processes that may have been visible when the sample was deformed to a lesser extent. Kamiyama *et al.* [39] proposed the decrease in magnetization of plastically deformed $MnPd_2Sn$ can be attributed to an APB with a displacement vector of $\mathbf{R} = \frac{a}{2}\langle 100\rangle$ (where a is the lattice parameter) that is generated and bound by the dissociation of a superdislocation with Burgers vector $\mathbf{b} = a\langle 100\rangle$ into two partial dislocations. Energetically favorable dissociation events similar to this proposed mecahnism can introduce defects within $MnAu_2Al$ that modify both local chemical order, and the interatomic distance between Mn atoms. This change in atomic structure could modify local magnetic ordering.

Our approach to resolving the structure and magnetic behavior induced by the plastic deformation of $MnAu_2Al$ is to search for likely defects in the material, and solve for the magnetic configuration these defects induce *via* DFT. Since the change in magnetic behavior is observed following plastic deformation, we examine the role of planar faults, which include APBs associated with stacking faults and dislocations. These planar faults are defined by the displacement of the perfect crystalline material along a plane, therefore deforming the crystal into two distinct regions, as shown in Fig. 5(a). Of the symmetrically distinct low-index planes present in the $L2_1$ structure of $MnAu_2Al$, relative displacements across the (010) and (110) planes can lead to APBs which preserve the lattice but change chemical order by permuting the Mn, Al, and Au sublattices. The on-lattice APBs which switch the Mn and Al sublattices are strong local minima, as can be seen in Fig. 5(b), indicating that dislocations induced by plastic deformation are likely to create these types of planar defects. The full γ-surface shown in Fig. 5(b) shows both the stacking fault energy (0.05 and 0.11 J/m^2), and the barrier required to reach these local minima (0.64 and 0.41 J/m^2) for the (010) and (110) planes, respectively, are well within the regime of mechanically accessible faults in a plastically soft material.

All low-energy APBs, which correspond to the exchange of Mn and Al sublattices across the (010) or (110) planes, induce a strong antiferromagnetic coupling across the fault. Figure 5(c) shows the relative energy of an antiferromagnetic configuration across the planar fault, as compared to preserving the ferromagnetic order of the pristine material. For small lattice displacements away from the pristine material, ferromagnetic order is preserved, but at the APBs, the antiferromagnetic configuration becomes stable.

The origin of the antiferromagnetic coupling across the interface is strongly antiferromagnetic Mn-Mn exchange interactions which are present only when one of the interacting Mn is on the Al or Au sublattice. To resolve these interactions, we compute all magnetic couplings present in this system, both in the pristine material and at on-lattice defects by constructing a cluster-expansion Hamiltonian which couples chemical and magnetic degrees of freedom on the underlying BCC lattice, as described in the methods. The

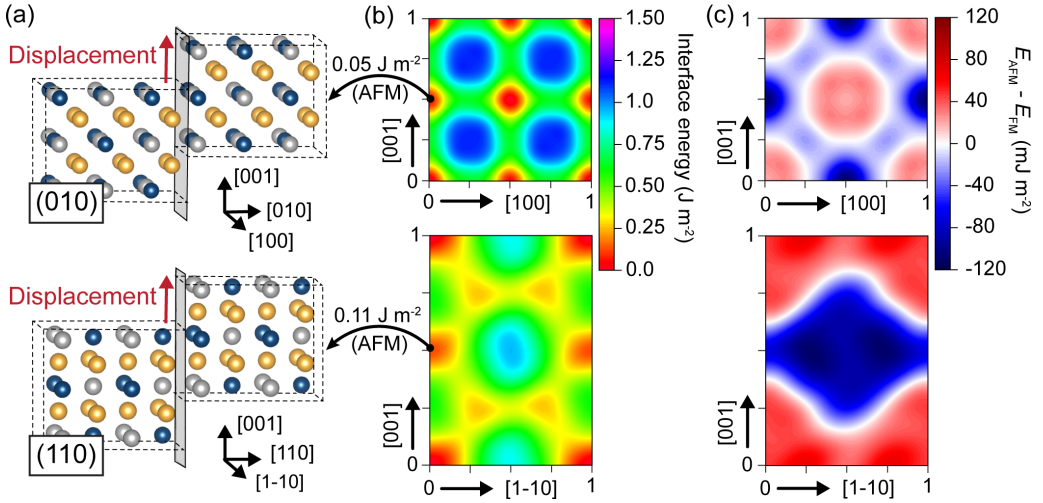

FIG. 5. Interfacial energy and magnetic configuration for planar faults in $MnAu_2Al$, as a function of the displacement vector in the (010) or (110) planes. (a) Atomic configuration of the low-energy APBs in the (010) and (110) planes, where the displacement vector in both cases is $a/2[001]$. (b) Interfacial energy of general planar faults (γ surface) in the (010) and (110) planes as a function of the displacement vector. (c) Relative energy of antiferromagnetic and ferromagnetic alignments across these interfaces.

magnetic component of the cluster expansion reveals that the sign and magnitude of Mn-Mn Heisenberg exchange strongly depends on the distance between the Mn atoms, and correspondingly, the sublattice on which each Mn resides. In pristine $L2_1$ $MnAu_2Al$, the dominant first and second nearest-neighbor interactions are ferromagnetic. Placing Mn on the Al sublattice results in two new couplings: a ferromagnetic nearest-neighbor interaction, and antiferromagnetic next-nearest neighbor interaction which is both larger in magnitude, and has a higher multiplicity. This pair of interactions determines the magnetic behavior of the low-energy APBs in the (010) and (110) planes—as the Mn and Al sublattices swap across the interface, the magnetic interactions are those corresponding to Mn_{Mn}-Mn_{Al}, which sum to give an antiferromagnetic coupling across the interface. Consistent with this picture, the cluster expansion model predicts that the lowest energy spin configurations for the interfaces given in Fig. 5(b) are collinear, with a magnetization reversal across the interface. Mn on the Au sublattice could also induce a strongly antiferromagnetic coupling, but this configuration is unlikely to be observed as evidenced by both the high energy of an isolated Mn_{Au} defect, and high energy of any stacking fault which permutes the Mn and Au sublattices. Finally, while the pristine Mn-Mn magnetic interactions may vary between the bulk and the interfacial region as depicted by the error bars in Fig. 6, these variations are too small to induce a qualitative change in magnetic order.

IV. CONCLUSIONS

The presence of exchange interactions are established here as being strongly coupled to chemical order to explain the acute sensitivity of the bulk magnetic moment in $MnAu_2Al$ to plastic deformation: dislocations lead to the formation of low-energy APBs in the (010) and (110) planes, which in turn force the magnetic moment to reverse across the dislocation and result in the disappearance of macroscopic magnetization. In contrast to magnetoelastic phenomena which are often controlled by weak spin-orbit interactions [40] and require the presence of large, spatially extended strain fields, we expect that this type of coupling between magnetism and plastic deformation is likely to be ubiquitous in ordered materials with multiple equivalent sublattices. Similarly, this coupling between the magnetism and chemical order implies that the magnetic configuration may be controlled either thermally, by controlling partial disorder in the material [41,42], or through engineering a dislocation network *via* the incorporation of

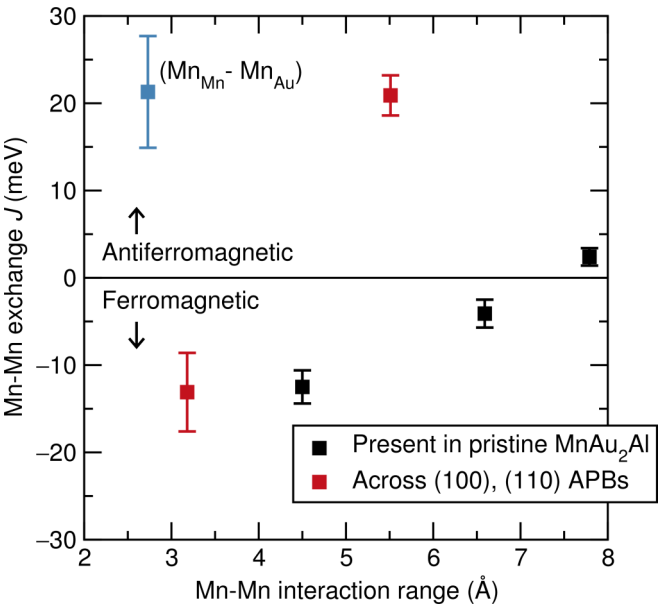

FIG. 6. Mn-Mn magnetic exchange as a function of interaction distance. The couplings present in pristine ordered $MnAu_2Al$ are predominantly ferromagnetic out to long range. At APBs, the change in chemical order results in Mn on the Al sublattice. While the nearest-neighbor Mn_{Mn}-Mn_{Al} interaction is ferromagnetic, the next-nearest-neighbor Mn_{Mn}-Mn_{Al} interaction is antiferromagnetic with a larger magnitude and interaction multiplicity, resulting in a net antiferromagnetic configuration across the APBs.

a precipitate phase [43]. The relative simplicity and large magnitude of this mechanism makes the further exploration of plasticity in ordered intermetallics a promising direction for obtaining mechanical control over magnetic behavior.

ACKNOWLEDGMENTS

This work was supported by the Materials Research Science and Engineering Center (MRSEC) program of the National Science Foundation (NSF) through DMR-1720256 (IRG-1), and employed the shared facilities of the MRSEC at UC Santa Barbara, a member of the Materials Research Facilities Network. We acknowledge the use of computing facilities from the Center for Scientific Computing (NSF Grant No. DMR1720256 and NSF Grant No. CNS-1725797), as well as the National Energy Research Scientific Computing Center, a Department of Energy (DOE), Office of Science User Facility supported by DOE Grant No. DE-AC02-05CH11231. Y.M.E. acknowledges the support of the Alexander von Humboldt Foundation through the Feodor Lynen Fellowship. J.A.M. is supported by the NSF Graduate Research Fellowship Program under NSF DGE-1650114.

[1] F. Heusler, W. Starck, and E. Haupt, Magnetisch-chemische studien, Verh. Deut. Phys. Ges. **5**, 219 (1903).

[2] T. Graf, C. Felser, and S. Parkin, Simple rules for the understanding of Heusler compounds, Prog. Solid State Chem. **39**, 1 (2011).

[3] T. Graf, S. S. P. Parkin, and C. Felser, Heusler compounds-a material class with exceptional properties, IEEE Trans. Magn. **47**, 367 (2010).

[4] J. Kübler, A. R. William, and C. B. Sommers, Formation and coupling of magnetic moments in Heusler alloys, Phys. Rev. B **28**, 1745 (1983).

[5] G. Malmström, D. J. W. Geldart, and C. Blomberg, Interaction between local magnetic moments in metals, J. Phys. F **6**, 1953 (1976).

[6] E. Şaşıoğlu, L. M. Sandratskii, and P. Bruno, Role of conduction electrons in mediating exchange interactions in Mn-based Heusler alloys, Phys. Rev. B **77**, 064417 (2008).

[7] E. Şaşıoğlu, L. M. Sandratskii, P. Bruno, and I. Galanakis, Exchange interactions and temperature dependence of magnetization in half-metallic Heusler alloys, Phys. Rev. B **72**, 184415 (2005).

[8] Y. Kurtulus, M. Gilleßen, and R. Dronskowski, Electronic structure, chemical bonding, and finite-temperature magnetic properties of full Heusler alloys, J. Comput. Chem. **27**, 90 (2006).

[9] Y. Noda and Y. Ishikawa, Spin waves in Heusler alloys Pd_2MnSn and Ni_2MnSn, J. Phys. Soc. Jpn. **40**, 690 (1976).

[10] K. Tajima, Y. Ishikawa, P. J. Webster, M. W. Stringfellow, D. Tocchetti, and K. R. A. Zeabeck, Spin waves in a Heusler alloy Cu_2MnAl, J. Phys. Soc. Jpn. **43**, 483 (1977).

[11] T. Shinohara, K. Sasaki, H. Yamaguchi, H. Wantanabe, and H. Sekizawa, On the reduction in magnetization by cold working on the ferromagnetic Heusler alloy Pd_2MnSn, J. Phys. Soc. Jpn. **50**, 2904 (1981).

[12] J. Schaf, K. L. Dang, P. Veillet, and I. A. Campbell, Extended and local effects of cold work in Heusler alloys, J. Phys. F **13**, 1311 (1983).

[13] A. J. Lapworth and J. P. Jakubovics, Effect of antiphase boundaries on the magnetic properties of Cu-Mn-Al Heusler alloys, Philos. Mag. **29**, 253 (1974).

[14] G. E. Bacon and E. W. Mason, The magnetic structures of the alloys $Au_2(Mn, Al)_2$, Proc. Phys. Soc. **92**, 713 (1967).

[15] W. Leiper, C. Blaauw, G. R. MacKay, and F. W. D. Woodhams, Mössbauer determination of the gold hyperfine field in the Heusler alloy Au_2MnAl, J. Phys. F **6**, 2191 (1976).

[16] D. P. Morris, R. R. Preston, and I. Williams, Search for new Heusler alloys, Proc. Phys. Soc. **73**, 520 (1959).

[17] D. P. Oxley, R. S. Tebble, and K. C. Williams, Heusler alloys, J. Appl. Phys. **34**, 1362 (1963).

[18] D. P. Morris and C. D. Price, The ferromagnetism of the Heusler alloy Au_2MnAl, Proc. Phys. Soc. **81**, 1074 (1963).

[19] K. Shirikawa, T. Kanomata, and T. Kaneko, Effect of hydrostatic pressure on the Curie temperature of the Heusler alloys Au_2MnAl and Pd_2MnZ (Z = Sn and Sb), J. Magn. Magn. Mater. **70**, 421 (1987).

[20] A. A. Coelho, TOPAS and TOPAS-Academic: An optimization program integrating computer algebra and crystallographic objects written in C++, J. Appl. Crystallogr. **51**, 210 (2018).

[21] D. Balzar, N. Audebrand, M. R. Daymond, A. Fitch, A. Hewat, J. I. Langford, A. Le Bail, D. Louër, O. Masson, N. McCowan, N. C. Popa, P. W. Stephens, and B. H. Toby, Size-strain line-broadening analysis of the ceria round-robin sample, J. Appl. Crystallogr. **37**, 911 (2004).

[22] G. Kresse and J. Hafner, *Ab initio* molecular dynamics for liquid metals, Phys. Rev. B **47**, 558 (1993).

[23] G. Kresse and J. Furthmüller, Efficiency of *ab-initio* total energy calculations for metals and semiconductors using a plane-wave basis set, Comput. Mater. Sci. **6**, 15 (1996).

[24] G. Kresse and J. Furthmüller, Efficient iterative schemes for *ab initio* total-energy calculations using a plane-wave basis set, Phys. Rev. B **54**, 11169 (1996).

[25] J. P. Perdew, K. Burke, and M. Ernzerhof, Generalized Gradient Approximation Made Simple, Phys. Rev. Lett. **77**, 3865 (1996).

[26] G. Kresse and D. Joubert, From ultrasoft pseudopotentials to the projector augmented-wave method, Phys. Rev. B **59**, 1758 (1999).

[27] S. P. Ong, W. D. Richards, A. Jain, G. Hautier, M. Kocher, S. Cholia, D. Gunter, V. L. Chevrier, K. A. Persson, and G. Ceder, Python Materials Genomics (pymatgen): A robust, open-source python library for materials analysis, Comput. Mater. Sci. **68**, 314 (2013).

[28] J. G. Goiri, multishifter package, Available at: https://github.com/goirijo/multishifter.

[29] D. A Kitchaev, E. C Schueller, and A. Van der Ven, Mapping skyrmion stability in uniaxial lacunar spinel magnets from first principles, Phys. Rev. B **101**, 054409 (2020).

[30] A. van de Walle and G. Ceder, Automating first-principles phase diagram calculations, J. Phase Equilib. **23**, 348 (2002).

[31] A. Van der Ven, J. C. Thomas, B. Puchala, and A. R. Natarajan, First-principles statistical mechanics of multicomponent crystals, Annu. Rev. Mater. Res. **48**, 27 (2018).

[32] S. Takahashi and T. Shinohara, Magnetic moment distribution in deformed Heusler alloy Pd_2MnSn, J. Phys. F **12**, 3115 (1982).

[33] G. Y. Chin, M. L. Green, R. C. Sherwood, and E. M. Gyorgy, Magnetic behavior of Heusler crystals disordered by plastic deformation, AIP Conf. Proc. **24**, 731 (1975).

[34] N. Takata, S.-H. Lee, C.-Y. Lim, S.-S. Kim, and N. Tsuji, Nanostructured bulk copper fabricated by accumulative roll bonding, J. Nanosci. Nanotechnol. **7**, 3985 (2007).

[35] Y. Saito, H. Utsunomiya, N. Tsuji, and T. Sakai, Novel ultra-high straining process for bulk materials-development of the accumulative roll-bonding (ARB) process, Acta Mater. **47**, 579 (1999).

[36] T. J. Nizolek, M. R. Begley, R. J. McCabe, J. T. Avallone, N. A. Mara, I. J. Beyerlein, and T. M. Pollock, Strain fields induced by kink band propagation in Cu-Nb nanolaminate composites, Acta Mater. **133**, 303 (2017).

[37] I. J. Beyerlein and L. S. Tóth, Texture evolution in equal-channel angular extrusion, Prog. Mater. Sci. **54**, 427 (2009).

[38] X. C. Liu, H. W. Zhang, and K. Lu, Formation of nano-laminated structure in nickel by means of surface mechanical grinding treatment, Acta Mater. **96**, 24 (2015).

[39] T. Kamiyama, T. Shinohara, S. Tomiyoshi, Y. Minonishi, H. Yamamoto, H. Asano, and N. Watanabe, Effect of deformation on Pd_2MnSn Heusler alloy studied with transmission electron microscopy, profile analysis of neutron powder diffraction pattern, and magnetization measurement, J. Appl. Phys. **68**, 4741 (1990).

[40] D. A. Kitchaev, I. J. Beyerlein, and A. V. der Ven, Phenomenology of chiral Dzyaloshinskii-Moriya interactions in strained materials, Phys. Rev. B **98**, 214414 (2018).

[41] E. Decolvenaere, M. Gordon, R. Seshadri, and A. V. der Ven, First-principles investigation of competing magnetic interactions in (Mn, Fe)Ru_2Sn Heusler solid solutions, Phys. Rev. B **96**, 165109 (2017).

[42] E. Decolvenaere, E. Levin, R. Seshadri, and A. Van der Ven, Modeling magnetic evolution and exchange hardening in disordered magnets: The example of $Mn_{1-x}Fe_xRu_2Sn$ Heusler alloys, Phys. Rev. Mater. **3**, 104411 (2019).

[43] Y. M. Eggeler, E. E. Levin, F. Wang, D. A. Kitchaev, A. Van der Ven, R. Seshadri, T. M. Pollock, and D. S. Gianola, Interfacial structure and strain accommodation in two-phase $NbCo_{1.2}Sn$ Heusler intermetallics, Phys. Rev. Materials **4**, 093601 (2020).